Bioinformatics, 2019, 1–10
doi: 10.1093/bioinformatics/btz401
Advance Access Publication Date: 16 May 2019
Original Paper

Bioimage informatics

Incorporating spatial–anatomical similarity into the VGWAS framework for AD biomarker detection

Meiyan Huang*, Yuwei Yu, Wei Yang, Qianjin Feng* and the Alzheimer's Disease Neuroimaging Initiative

Guangdong Provincial Key Laboratory of Medical Image Processing, School of Biomedical Engineering, Southern Medical University, Guangzhou 510515, China

*To whom correspondence should be addressed.

Associate Editor: Robert Murphy

Received on December 26, 2018; revised on April 3, 2019; editorial decision on May 3, 2019; accepted on May 7, 2019

Abstract

Motivation: The detection of potential biomarkers of Alzheimer's disease (AD) is crucial for its early prediction, diagnosis and treatment. Voxel-wise genome-wide association study (VGWAS) is a commonly used method in imaging genomics and usually applied to detect AD biomarkers in imaging and genetic data. However, existing VGWAS methods entail large computational cost and disregard spatial correlations within imaging data. A novel method is proposed to solve these issues.

Results: We introduce a novel method to incorporate spatial correlations into a VGWAS framework for the detection of potential AD biomarkers. To consider the characteristics of AD, we first present a modification of a simple linear iterative clustering method for spatial grouping in an anatomically meaningful manner. Second, we propose a spatial–anatomical similarity matrix to incorporate correlations among voxels. Finally, we detect the potential AD biomarkers from imaging and genetic data by using a fast VGWAS method and test our method on 708 subjects obtained from an Alzheimer's Disease Neuroimaging Initiative dataset. Results show that our method can successfully detect some new risk genes and clusters of AD. The detected imaging and genetic biomarkers are used as predictors to classify AD/normal control subjects, and a high accuracy of AD/normal control classification is achieved. To the best of our knowledge, the association between imaging and genetic data has yet to be systematically investigated while building statistical models for classifying AD subjects to create a link between imaging genetics and AD. Therefore, our method may provide a new way to gain insights into the underlying pathological mechanism of AD.

Availability and implementation: https://github.com/Meiyan88/SASM-VGWAS.

Contact: huangmeiyan16@163.com or 1271992826@qq.com

1 Introduction

Alzheimer's Disease (AD), a common form of dementia in elderly people, gradually destroys brain regions that are responsible for memory, learning, thinking and behavior (Alzheimer's Association, 2016). Before dementia is clinically diagnosed, pathologic processes leading to this progressive neurodegenerative disorder begin (Chauhan *et al.*, 2015). Therefore, the early detection of AD may largely improve the treatment of AD, and many groups focus on finding AD biomarkers in different ways (Ning *et al.*, 2018; Zhang *et al.*, 2014). Various biomarkers have been investigated for AD detection through different techniques, such as structural brain magnetic resonance imaging (MRI) (Frisoni *et al.*, 2010), positron

emission tomography (PET) (Santi *et al.*, 2001), cerebrospinal fluid (CSF) (Mattsson *et al.*, 2009) and genetic data (Lambert *et al.*, 2013). AD is characterized by specific brain structural changes and genetic risk factors (Ning *et al.*, 2018; Weiner *et al.*, 2015). On the one hand, measurements of structural changes based on brain MRI images have commonly been used for AD-associated analysis, indicating that MRI can contribute to the understanding of AD-related neural changes (Chauhan *et al.*, 2015; Huang *et al.*, 2017b; Ning *et al.*, 2018; Zhuo *et al.*, 2018). On the other hand, AD risk is affected by genetic variants an individual carries, which can be measured accurately from birth (Lambert *et al.*, 2013). As such, detecting AD biomarkers from structural brain MRI and genetic data is a potential way for the early prediction, diagnosis and treatment of AD (Ning *et al.*, 2018; Zhang *et al.*, 2014).

Imaging genetics has emerged as a new field to detect potential imaging and genetic biomarkers of AD and help discover remarkable but hidden associations between causal genes and specific variations in brain regions in AD for developing new treatments, monitoring treatment effectiveness and shortening the duration of clinical trials (Chauhan *et al.*, 2015; Huang *et al.*, 2015, 2017; Stein *et al.*, 2010). To date, the main approach of detecting genetic effects on structural brain MRI images in imaging genetics is voxel-wise genome-wide association study (VGWAS), which is applied to detect potential biomarkers of diseases by combining multiple phenotypic variables (e.g. voxels in an imaging space) and whole genomes [e.g. single nucleotide polymorphism (SNP)] (Huang *et al.*, 2015; Li *et al.*, 2012; Stein *et al.*, 2010). In contrast to methods involving candidate phenotypes or genotypes, VGWAS does not require prior knowledge of disease pathology to select candidate phenotypes and genotypes; thus, VGWAS can reduce the probability of missing important genes and brain clusters (Huang *et al.*, 2015). However, several problems existing in VGWAS should be considered. First, running VGWAS poses remarkable computational challenges because it usually runs genome-wide ($N_G \sim 10^6$ known variants) associations with signals at millions of locations ($N_V \sim 10^6$) in the brain (Huang *et al.*, 2015, 2017). Specifically, elements in a search space in VGWAS are about $N_G N_V (\sim 10^{12})$. To solve this problem and accelerate the calculation of traditional VGWAS, we proposed a fast voxel-wise genome-wide association analysis (FVGWAS) in our previous study (Huang *et al.*, 2015).

Second, most VGWAS methods, including our FVGWAS method, are standard voxel-wise methods that treat each voxel as an individual unit and disregard the spatial correlations of imaging data. With the inherent biological structure and function of objects, imaging data are spatially correlated in nature and contain spatially contiguous regions with sharp edges (Huang *et al.*, 2015; Zhu *et al.*, 2014). Such spatial correlations can be essential for the accurate estimation of VGWAS. Gaussian smoothing with a prefixed bandwidth is a fast, easily adjusted and commonly used method to incorporate imaging spatial correlations into VGWAS (Huang *et al.*, 2019). However, imaging data near the edges of important regions are usually blurred when Gaussian method is used, thereby leading to an increase in the number of false positives and negatives and a decrease in statistical accuracy (Li *et al.*, 2012, 2013). Moreover, Li *et al.* (2012) developed a multiscale adaptive regression method for the spatial analysis of imaging data in VGWAS and found that their method is more effective than traditional VGWAS. However, the computational cost of multiscale adaptive regression method is higher than that of traditional VGWAS (Li *et al.*, 2012), which is not computationally feasible even for thousands of SNPs (Huang *et al.*, 2015). A Functional genome-wide association analysis method (Huang *et al.*, 2017) has also been presented to exploit spatial correlations in imaging data, and this method effectively improves the detection accuracy of AD biomarkers in VGWAS. Therefore, spatial correlations in imaging data are important for disease-associated biomarker detection in VGWAS.

In this study, we introduce an alternative strategy to incorporate spatial correlations into a VGWAS framework for potential AD biomarker detection. On the one hand, spatial correlations between voxels are important in VGWAS. On the other hand, anatomical features related to AD should be considered when spatial correlations are incorporated into the VGWAS framework because AD is highly associated with specific brain structural changes (Ning *et al.*, 2018; Weiner *et al.*, 2015). Therefore, our goal is to incorporate the spatial correlations based on not only the neighboring voxels in imaging data but also the anatomical features associated with AD to improve the biomarker detection ability of the VGWAS method. To achieve this goal, we first introduce a modification of simple linear iterative clustering (SLIC) (Achanta *et al.*, 2012) for spatial grouping in an anatomically meaningful manner. We also propose a spatial–anatomical similarity matrix (SASM) to incorporate correlations among voxels. Finally, we detect potential AD biomarkers from imaging and genetic data by using the FVGWAS method, which can considerably reduce the computational cost. To validate our method, we perform a set of experiments on 708 subjects, and each subject has a total of 193 275 voxels and 501 584 SNPs. In the experiments, we successfully detect some new AD-associated risk genes, such as SPON1, CTNNA2, CTNND2 and ZNF407. We then use the detected imaging and genetic biomarkers as predictors to classify AD/normal control (NC) subjects and achieve a high accuracy of AD/NC classification. To the best of our knowledge, no research has systematically investigated the association between imaging and genetic data while building statistical models for classifying AD subjects to create a link between imaging genetics and AD. Therefore, the proposed method may provide a new way to gain insights into the underlying pathological mechanism of AD.

2 Materials

In preparation for our analysis, the genetic data and structural MRI scans of the human brain were obtained from the Alzheimer's Disease Neuroimaging Initiative (ADNI) database (http://adni.loni.usc.edu/). ADNI was launched in 2003 by the National Institute on Aging, the National Institute of Biomedical Imaging and Bioengineering, the Food and Drug Administration, private pharmaceutical companies and non-profit organizations, as a $60 million, 5-year public–private partnership. The primary goal of ADNI has been to test whether serial MRI, PET and other biological markers are useful in clinical trials of mild cognitive impairment (MCI) and early AD. Determination of sensitive and specific markers of very early AD progression is intended to aid researchers and clinicians to develop new treatments and monitor their effectiveness, as well as lessen the time and cost of clinical trials. ADNI subjects aged 55–90 from over 50 sites across the USA and Canada participated in the research and more detailed information is available at www.adni-info.org.

Data from 708 (421 men and 287 women, age 75.61 ± 6.76 years) subjects with the structural MRI data of 164 AD, 346 MCI and 198 NC provided by the ADNI dataset were used. These MRI data were obtained on a 1.5 T MRI scanner by using a 3D MPRAGE sequence in the sagittal plane. The scan parameters were as follows: repetition time was 2400 ms; inversion time was 1000 ms; flip angle was 8° and field of view was 24 cm with a

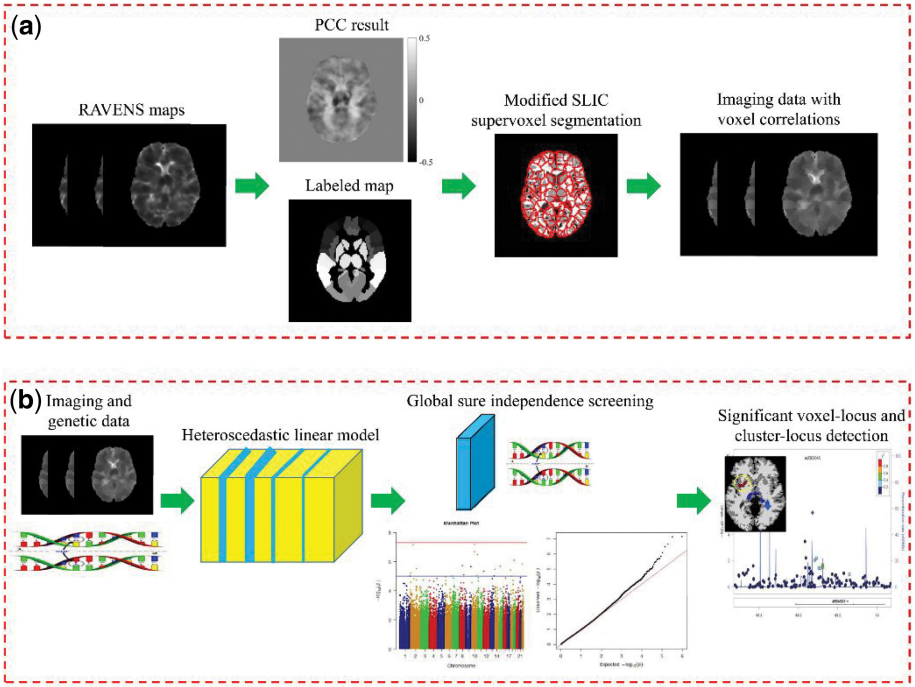

Fig. 1. Overview of our proposed method. (**a**) Incorporating voxel correlations in imaging data. (**b**) Detecting biomarkers from imaging and genetic data by using the FVGWAS method

256 × 256 × 170 acquisition matrix (*x*-, *y*- and *z*-dimensions), which yielded a voxel size of 1.25 × 1.26 × 1.2 mm^3.

The standard processing approach that we used for the MRI data involved the following: (i) use of a non-parametric non-uniform bias correction (N3) for image intensity inhomogeneity correction (Sled *et al.*, 1998); (ii) skull stripping (Wang *et al.*, 2014) and warping a labeled template to each skull-stripped image for the removal of the cerebellum (aBEAT in version 1.0, http://www.nitrc.org/projects/abeat); (iii) segmentation of each brain image into four different tissues, namely, white matter (WM), gray matter (GM), CSF and ventricles, via the FAST method (Zhang *et al.*, 2001) (FAST in FMRIB Software Library version 5.0, https://fsl.fmrib.ox.ac.uk/fsl/fslwiki/); (iv) registration of all images to the common template by using the 4D-HAMMER method proposed in a previous study (Shen and Davatzikos, 2004) (HAMMER in version 1.0, https://www.nitrc.org/projects/hammer/); (v) use of the deformation field to generate the RAVENS maps (Davatzikos *et al.*, 2001), which can be used to quantify the local volumetric group differences in the whole-brain volume and in each tissue type (WM, GM, CSF and ventricles) and (vi) automatically labeling of 90 regions of interest (ROIs) on the template (Tzourio-Mazoyer *et al.*, 2002) defined as labeled map A, which would be used in supervoxel calculation (Section 3.2.1).

We used the Human 610-quad Beadchip (Illumina, Inc., San Diego, CA) to acquire the genotype data of 818 subjects, including 620 901 SNPs, which were provided by the ADNI dataset. To avoid the effect of population stratification, we utilized 749 Caucasians selected from the 818 subjects with genetic data and imaging data at the baseline in our study. Then, we performed quality control procedures (QCPs), including the steps presented below, to exclude unsatisfactory data through (i) gender check; (ii) population stratification; (iii) sibling pair identification; (iv) call rate check for each subject and each SNP marker; (v) marker removal according to minor allele frequency and (vi) Hardy–Weinberg equilibrium test. Next, we screened the SNPs for the following: (i) at least 95% retention values; (ii) at least 95% minor allele frequency and (iii) Hardy–Weinberg equilibrium $P > 10^{-6}$. We inputted the remaining missing genetic data as the modal value. After conducting the quality control procedures and SNP screening, we retained 708 subjects, and each subject had 501 584 SNPs during the subsequent analysis.

3 Method

Figure 1 presents an overview of our proposed method that consists of two modules for detecting potential biomarkers. The first module (Fig. 1a) shows the process of incorporating voxel correlations in imaging data. The second module (Fig. 1b) demonstrates how to detect biomarkers from imaging and genetic data by using the FVGWAS method. The details of our proposed method are provided in the following subsections.

3.1 Mathematical formulation

We consider n independent subjects, and each subject is associated with a set of imaging data, clinical variables and genetic markers. Let V be a selected brain region that contains N_V voxels, and let v be a voxel in V ($v \in V$). Let G be the set of genetic loci containing N_G SNPs and let g be a locus in G ($g \in G$). For each individual $i (i = 1, \ldots, n)$, the following parameters are considered: an $N_V \times 1$ vector of image measurement denoted by $\mathbf{Y}_i = \{y_i(v)\}$, a $D \times 1$ vector of clinical covariates $\boldsymbol{x}_i = (x_{i1}, \ldots, x_{iD})^T$, and an $L \times 1$ vector $z_i(g) = (z_{i1}(g), \ldots, z_{il}(g), \ldots, z_{iL}(g))^T$ for genetic data at locus g, where z_{il} and L are the l-th genetic data and the dimension of genetic data, respectively.

3.2 SASM

To incorporate correlations between voxels into VGWAS, we introduce a SASM to incorporate the correlations between voxels into VGWAS:

$$W = \{w(v,v'); (v,v') \in V\}, \ \text{s.t.} w(v,v') \geq 0, \ \sum_{v' \in N(v)} w(v,v') = 1 \quad (1)$$

where $N(v)$ is a set of neighboring voxels of v and $w(v,v')$ represents the similarity between voxel v and the voxel v' in $N(v)$. The size of $N(v)$ should be determined to calculate SASM. Although defining $w(v,v')$ for all combinations of (v,v') is conceptually possible, holding such a large matrix with $O(N_V^2)$ in memory is computationally difficult for most personal computers. However, small neighboring voxel sets, such as 6 or 26 neighboring voxels, may lose some crucial correlations between voxels because disease-induced structural changes may occur in some relatively large regions of the brain (Huang *et al.*, 2017). Therefore, considering the anatomy knowledge associated with AD, we first propose a modified SLIC supervoxel segmentation method (Zhuo *et al.*, 2018) to determine the neighboring voxel set $N(v)$ for each voxel v. Subsequently, we provide the formulation of SASM with the calculated neighboring voxel sets. Notably, either modified SLIC or SASM exploits the disease-related information across all subjects to generate $N(v)$ vectors, each of which consists of weights between voxel v and the voxels in $N(v)$. These weights are in turn fed back into the MRI images for each subject to incorporate spatial correlations. Specifically, n MRI images share weights at the same voxel site.

3.2.1 Anatomically constrained supervoxels for $N(v)$ definition

Determining the size of $N(v)$ can be treated as a voxel grouping problem. Applying the image preprocessing step (Section 2), we obtain the grouping of voxels in the template space based on anatomical structures. However, anatomy-based grouping may be suboptimal because information may be hidden in subregional parts of the anatomy (Zhuo *et al.*, 2018). Supervoxel method has been successfully used in medical image analysis (Fan *et al.*, 2007; Zhuo *et al.*, 2018), which can be used to group voxels into perceptually meaningful atomic regions. Therefore, we incorporated the supervoxel method and anatomical boundaries into the VGWAS framework to explore voxel correlations.

In this study, we introduce a modification of the SLIC supervoxel segmentation method as mentioned in a previous study (Zhuo *et al.*, 2018), which considered anatomical boundaries. In contrast to most supervoxel methods, which group voxels based on image intensity, we use the correlation of the voxel intensity with the disease label, which is widely used in AD prediction to obtain the correlation between images and disease labels (Rathore *et al.*, 2017; Zhuo *et al.*, 2018), to group voxels. For each voxel site, we first compose a vector with the intensity values at the voxel site across all subjects. Then, we compute the Pearson correlation coefficient (PCC) between this vector and the disease labels, obtaining a volume of correlation values at each voxel. We use AD and NC subjects rather than MCI subjects to calculate the PCC volume because MCI can be regarded as an intermediate stage between AD and NC and has the characteristics of both AD and NC (Liu *et al.*, 2015). To prevent the supervoxels from crossing anatomical boundaries, we introduce an additional cost to the cost function proposed in the SLIC method. For each supervoxel k, we define the modified cost function as follows:

$$\min_{C_k} D(P,A,C_k,v) = \min_{C_k} \sqrt{\left(\frac{d_c(P,C_k,v)}{m}\right)^2 + \left(\frac{d_s(C_k,v)}{S}\right)^2} + d_a(A,C_k,v) \quad (2)$$

where $d_c(P,C_k,v) = \|P(v) - P(v_{C_k})\|_2$ and $d_s(C_k,v) = \|v - v_{C_k}\|_2$ are the content-based and spatial distances defined in SLIC, respectively (Achanta *et al.*, 2012). $\|\cdot\|_2$ represents the Euclidean norm, and P is the input image, whose image measurement is PCC instead of intensity. In addition, C_k and v_{C_k} represent the voxel set of k and the supervoxel center of k, respectively, and $S = \sqrt[3]{N_V/K}$ is the sampling interval for 3D volume, where K is the supervoxel number. m is a constant value and can be used to weigh the relative importance between content similarity and spatial proximity (Achanta *et al.*, 2012). When m is large, spatial proximity is important, and the resulting supervoxels are compact. When m is small, the resulting supervoxels are tightly to image boundaries (Achanta *et al.*, 2012). In our study, we empirically set $m = 40$ in accordance with previously described methods (Wang *et al.*, 2016) and add the cost $d_a(A,C_k,v)$, which is the distance based on an available anatomical label map A. To constrain a supervoxel to be part of one anatomical region, we define $d_a(A,C_k,v)$ as follows:

$$d_a(A,C_k,v) = \begin{cases} 0 & if \quad A(v) = A(v_{C_k}) \\ \infty & otherwise \end{cases} \quad (3)$$

where $A(v)$ and $A(v_{C_k})$ are the anatomical labels at voxel v and supervoxel center v_{C_k}, respectively. Each voxel v is assigned to C_k that minimizes the cost function D in Equation (2). Therefore, in accordance with the definitions of Equations (2) and (3), each v is assigned to C_k that satisfies the condition $A(v) = A(v_{C_k})$. For the anatomical label map A, we use an automatically labeled result on the template (Section 2). With the calculated $\{C_k\}_{k=1}^K$ of K supervoxels, the neighboring voxel set $N(v)$ of each voxel v can be defined as $N(v) = \{C_k \setminus v; v \in C_k\}$.

3.2.2 Formulation of SASM

After determining the $N(v)$, how to calculate the shared weight $w(v,v')$ is a problem to be solved. As we mentioned above, pathological changes of AD in the brain are commonly observed in a region not merely in an isolated voxel. Moreover, the voxels within the same region, such as our proposed supervoxels, show similar values in terms of intensities in MRI. The similarities among voxels in a region depend on distance and intensity. Thus, proposing SASM is reasonable to formulate the similarities between voxel v and the voxel v' in $N(v)$. Moreover, the neighboring voxel set $N(v)$ of voxel v is defined on the basis of anatomical map A, which labels the AD-related ROIs. Hence, our proposed SASM considers both similarities among voxels and anatomical features associated with AD. In SASM, the weight $w(v,v')$ decreases when the distance or the difference in intensities between voxel v and v' increases. We define $w(v,v')$ as follows:

$$w(v,v') = \frac{\tilde{w}(v,v')}{\sum_{v' \in N(v)} \tilde{w}(v,v')} \ \text{with} \ \tilde{w}(v,v') = I_1(v,v') I_2(v,v') \quad (4)$$

where $I_1(v,v') = \exp\left(-\|v - v'\|_2 / h_1\right)$ and $I_2(v,v') = \exp\left(-K(v,v')/\ h_2\right)$. Moreover, $K(v,v')$ is a function of (v,v') and can be defined as follows:

$$K(v,v') = median^2\left(\left\{\frac{y_i(v)-y_i(v')}{\sqrt{var(\mathbf{Y}(v)-\mathbf{Y}(v'))}}\right\}_{i=1\cdots n}\right). \quad (5)$$

In Equations (4) and (5), $I_1(v,v')$ represents the similarity of distance between voxels v and v', while $I_2(v,v')$ represents the similarity of intensity. In contrast to $I_1(v,v')$, $I_2(v,v')$ across all subjects are usually different from each other. To minimize the effect of outliers and maintain consistency in the MRI images, we use the squared median of normalized differences in intensities to describe the unified difference in intensities between voxels v and v'.

On a macroscopic level, the shared weights w that formulate the similarities among voxels based on anatomical boundaries, reflect the spatial correlations within the imaging data by virtue of I_1 and I_2. With the calculated weights $w(v,v')$, voxel correlation information can be incorporated by using the following formulation:

$$y_{i,w}(v) = \sum\nolimits_{v'\in N(v)} w(v,v')y_i(v). \quad (6)$$

3.3 FVGWAS framework

The FVGWAS method is proposed to efficiently carry out whole-genome analyses of whole-brain data (Huang *et al.*, 2015). Here, we briefly introduce the FVGWAS framework, and further details are provided in another study (Huang *et al.*, 2015).

A heteroscedastic linear model can be written as follows:

$$y_{i,w}(v) = \boldsymbol{x}_i^T\boldsymbol{\beta}_{\mathrm{w}}(v) + \boldsymbol{z}_i(g)^T\boldsymbol{\gamma}_{\mathrm{w}}(g,v) + e_{i,w}(v) \quad (7)$$

where $\boldsymbol{\beta}_{\mathrm{w}}(v)$ and $\boldsymbol{\gamma}_{\mathrm{w}}(g,v)$ are coefficients associated with non-genetic predictors and genetic effects, respectively, and $e_{i,w}(v)$ is a measurement error.

In model (7), a hypothesis testing problem on $\boldsymbol{\gamma}_{\mathrm{w}}(g,v)$ can be expressed as follows:

$$H_0:\ \boldsymbol{\gamma}_{\mathrm{w}}(g,v) = \mathbf{0} \text{ versus } H_1:\ \boldsymbol{\gamma}_{\mathrm{w}}(g,v) \neq \mathbf{0} \text{ for each } (g,v) \quad (8)$$

where H_0 indicates that genetic data are not associated with image data. To test if $\boldsymbol{\gamma}_{\mathrm{w}}(g,v)$ =0, we can calculate a Wald-type statistic:

$$W(g,v) = \tilde{\boldsymbol{\gamma}}_w(g,v)^T\left\{Cov(\tilde{\boldsymbol{\gamma}}_w(g,v))\right\}^{-1}\tilde{\boldsymbol{\gamma}}_w(g,v) \quad (9)$$

where $\tilde{\boldsymbol{\gamma}}_w(g,v)$ is the ordinary least squares estimate of $\boldsymbol{\gamma}_{\mathrm{w}}(g,v)$. However, the calculation of $W(g,v)$ for all (g,v) pairs is computationally intensive. To solve this problem, we introduce a global sure independence screening (GSIS) procedure via the FVGWAS method to speed up the calculation. The key idea of the GSIS procedure in FVGWAS is to detect potentially causal genetic markers by using a dimension reduction method and an approximation method (Huang *et al.*, 2015). Specifically, a global Wald-type statistic can be used to eliminate many loci with weak or even no genetic effects because only a small number of causal genetic markers are expected to contribute to the image measurements (Huang *et al.*, 2015, 2017):

$$W(g) = N_V^{-1}\sum_{v\in V} W(g,v). \quad (10)$$

We can calculate the P-values of $W(g)$ in all of the loci by using an approximation method (Huang *et al.*, 2015; Zhu *et al.*, 2012). Finally, we can select the top N_0 loci with the highest $-\log_{10}(p)$ − values, and the selected N_0 loci can be denoted as $\tilde{G}_0 = \left\{\tilde{g}_0,\ldots,\tilde{g}_{N_0}\right.$ and used to construct a candidate significant locus set.

For the detection procedure, two wild bootstrap methods are used. The first one is to detect the imaging phenotypic measures (voxels) that are significantly associated with the selected N_0 loci. The second one is to detect the subregions or clusters of the imaging phenotype significantly associated with the selected N_0 loci. Significant voxel–locus pairs for VGWAS should be selected, but such detection is less meaningful for the proposed method, whose voxel correlation information has been incorporated into the FVGWAS framework. Important genetic markers should be associated with relatively large ROIs in biologically (Huang *et al.*, 2015). Therefore, existing VGWAS methods for imaging phenotypes focus on the first detection step, whereas we are particularly interested in the second detection step. In a previous work (Huang *et al.*, 2015), wild bootstrap method can prevent the repeated analyses of simulated datasets. As such, it can considerably reduce computational time.

4 Experimental results

In the ADNI data analysis, we use RAVENS maps as phenotypes to evaluate the performance of the proposed method with 708 subjects (164 AD, 346 MCI and 198 NC). Each subject has 193 275 voxels and 501 584 SNPs. The clinical covariates include age, gender, intercept, whole-brain volume and top five principal component scores for the SNPs. In the experiments, we first optimize the parameters in the proposed method with 164 AD and 198 NC subjects. Thereafter, we perform the proposed method with the optimized parameters on imaging and genetic data of 708 subjects to detect AD-related biomarkers. In the following sections, we will provide the details of parameter optimization and biomarker detection of the proposed method.

4.1 Parameter optimization

In this study, K is a crucial parameter utilized to determine the size of $N(v)$ for each v. However, selecting an optimal K is difficult because we have no ground truth of the biomarkers associated with AD in imaging and genetic data. The accurate prediction and diagnosis of AD is the final target of AD-associated biomarker detection. Therefore, we may consider using the detected biomarkers as predictors of AD diagnosis. We choose K from 500; 1000; 1500; 2000; 2500 and 3000 through a 5-fold cross-validation method and evaluate the proposed method on 164 AD and 198 NC subjects, excluding MCI subjects, to classify these subjects into AD and NC. Specifically, we divide all AD and NC subjects into five subsets with the same proportion of each class label. For each run of the 5-fold cross-validation, we successively choose one of the five subsets as a testing set and combine the remaining four subsets to be a training set. By varying the values of K in the proposed method, we can obtain different $\{C_k\}_{k=1}^K$ in the training set. Thereafter, we can utilize the obtained $\{C_k\}_{k=1}^K$ to calculate $N(v)$, $w(v,v')$, and $y_{i,w}(v)$. Subsequently, we can apply the FVGWAS method to detect AD-associated imaging and genetic biomarkers and use these two types of biomarkers, respectively, as predictors to train a classifier. With the trained classifiers, we use the detected biomarkers in the testing set as classifier inputs to obtain the classification results. Therefore, for each K value, we can obtain five classification results for the 5-fold cross-validation and achieve a classification accuracy by averaging the five classification results. The value of K with the best mean classification accuracy on the testing set will be chosen. In this study, we apply a support vector machine (SVM) as a classifier, considering its typical use for AD classification (Liu *et al.*, 2015; Zhang

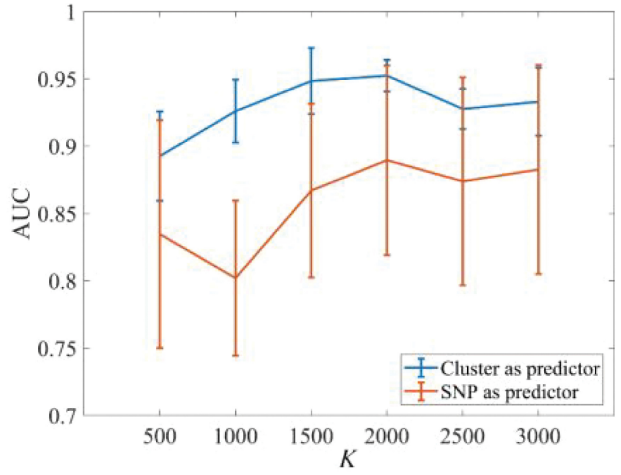

Fig. 2. Accuracy (measured as area under the receiver operating characteristic curves) of different K with clusters or loci as predictors in AD/NC classification. Clusters and loci are the significant voxel set and the significant loci detected by the proposed method, respectively

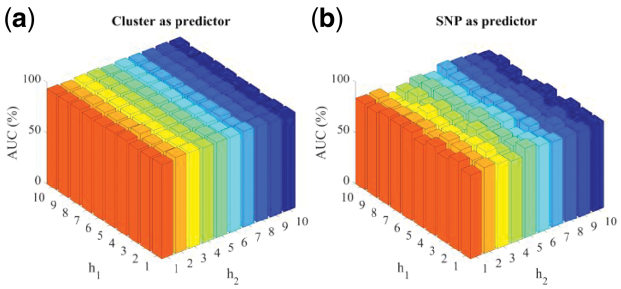

Fig. 3. Accuracy (measured as area under the Receiver Operating Characteristic curves) of different h_1 and h_2 with clusters (**a**) or loci (**b**) as predictors in AD/NC classification

et al., 2014; Zhuo *et al.*, 2018). To make a fair comparison, we carefully design and select the parameters with optimal performance in each SVM classifier in the experiments. Similarly, the parameters h_1 and h_2 in weight $w(v, v')$ calculation are chosen from $\{1, 2, \ldots, 10$ through cross-validation on AD and NC subjects.

In the experiments, we vary the value of K from 500; 1000; 1500; 2000; 2500 and 3000 and then record the corresponding AD/NC classification results. Parameters h_1 and h_2 in $w(v, v')$ calculation are fixed at 4 and 2, respectively. Moreover, loci number N_0 in the candidate significant locus set is set to 1000. Figure 2 shows the classification results of imaging and genetic biomarkers with different K values. Figure 2 depicts that the classification accuracy is improved by an increase in K, except when SNP is used as a predictor at $K = 1000$. In addition, the classification accuracy reaches its highest value when $K = 2000$. Thus, K is fixed at 2000 for the subsequent experiments.

Furthermore, parameters h_1 and h_2 are varied from $\{1, 2, \ldots, 10$ to test the classification performance. In this experiment, K and N_0 are fixed to 2000 and 1000, respectively. Figure 3 presents the experimental results. The figure further shows that the classification accuracies of different h_1 and h_2 with clusters or loci as predictors slightly fluctuate in a small range with the varieties of h_1 and h_2, indicating that the classification accuracies achieved by the proposed method are generally stable with respect to these two parameters. Therefore, h_1 and h_2 are set to 4 and 2, respectively, which have a slightly higher classification accuracy than other values in using cluster or loci as predictors, in the subsequent experiments.

Table 1. Accuracy (ACC) and area under the receiver operating characteristic curves (AUC) of the proposed method and the FVGWAS method

	Cluster as predictor		SNP as predictor	
	ACC	AUC	ACC	AUC
Proposed method	0.901±0.031	0.952±0.012	0.810±0.060	0.883±0.078
FVGWAS	0.846±0.065	0.922±0.026	0.758±0.070	0.823±0.075

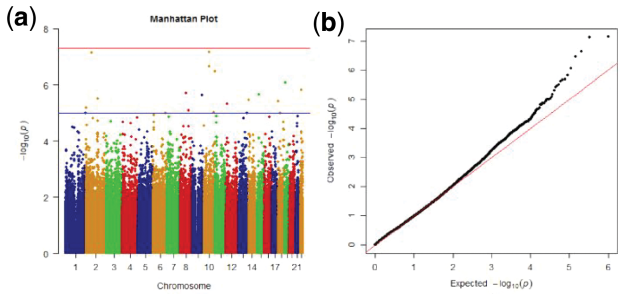

Fig. 4. (**a**) Manhattan and (**b**) QQ plots of ADNI whole-brain VGWAS

4.2 Comparison with FVGWAS method

The proposed method is compared with the FVGWAS method to evaluate the effectiveness of incorporating voxel correlations into the FVGWAS framework. In this experiment, K, h_1 and h_2 in the proposed method is fixed at 2000, 4 and 2, respectively, and a 5-fold cross-validation method is used to evaluate the proposed method and the FVGWAS method in AD/NC classification. The SVM classifier is also applied to obtain the classification results. For fair comparison, the SVM parameters are carefully designed and selected to achieve the optimal performance of these two methods. In this experiment, N_0 is set to 1000 for different methods. Table 1 shows the classification accuracy of the proposed method and the FVGWAS method. Table 1 also shows that the performance of the proposed method is better than that of the FVGWAS method with either imaging data (clusters) or genetic data (SNP) as predictors ($pP < 0.5$, pair t-test).

4.3 Biomarker detection

In this section, our goal is to examine the genetic effect of each of the 501 584 SNPs on the whole brain and detect some potential biomarkers associated with AD. To achieve this goal, we use the proposed method on the RAVENS maps and SNP data of 708 subjects (164 AD, 346 MCI and 198 NC) and set K, h_1 and h_2 to 2000, 4 and 2, respectively.

With the GSIS procedure, the P-values of $W(g)$ of all of the loci are computed. Figure 4 shows the Manhattan and QQ plots of the VGWAS results of the RAVENS maps. The Manhattan plot (Fig. 4a) is a plot of the $-\log_{10}(p)$ − values of the association statistic on the y-axis versus the chromosomal position of the SNP on the x-axis. SNPs with high $-\log_{10}(p)$ − values represent their high associations with traits (ADNI brain image measurement in this study). As shown in Figure 4a, 20 SNPs are associated with the whole brain

Table 2. ADNI whole-brain VGWAS: top 50 selected SNPs associated with the whole brain. '- -' in the table indicates the item was not found to correspond to genes

SNP	CHR	BP	*P*-value	Gene	SNP	CHR	BP	*P*-value	Gene
rs11815438	10	62 501 737	7.05E-08	LOC105378320	rs11731185	4	177 123 850	1.49E-05	–-
rs11891634	2	65 926 939	7.14E-08	–-	rs17017837	2	79 995 904	1.50E-05	CTNNA2
rs1060373	10	62 554 500	2.18E-07	CDK1	rs1146888	13	76 887 683	1.51E-05	–-
rs2480271	10	132 061 197	3.33E-07	–-	rs1405933	2	140 829 708	1.90E-05	–-
rs10402592	19	11 256 887	8.49E-07	SPC24	rs11717277	3	54 220 871	1.99E-05	CACNA2D3
rs5994978	22	34 988 594	1.51E-06	–-	rs989707	4	5 210 283	2.10E-05	STK32B
rs7001339	8	69 855 507	2.00E-06	LINC01592	rs853363	6	14 138 858	2.13E-05	–-
rs4924156	15	37 688 630	2.17E-06	LOC105370772	rs1014824	18	64 667 804	2.15E-05	–-
rs12001550	9	120 672 883	2.30E-06	–-	rs1528663	11	13 967 222	2.19 E-05	–-
rs13419007	2	145 043 653	3.12E-06	GTDC1	rs2830706	21	28 487 190	2.35 E-05	–-
rs17182599	14	22 051 519	3.44E-06	–-	rs971752	4	103 224 534	2.36 E-05	SLC39A8
rs11872654	18	2 164 155	3.81E-06	–-	rs16857117	2	11 205 421	2.74 E-05	–-
rs9645752	12	12 544 266	4.84E-06	BORCS5	rs1325998	10	4 092 494	2.94 E-05	LOC107984195
rs1448575	2	6 386 393	6.59E-06	–-	rs2697880	8	37 227 905	3.06 E-05	–-
rs2514323	8	99 236 899	7.98E-06	NIPAL2	rs2443568	8	99 254 045	3.11 E-05	NIPAL2
rs2935713	10	123 432 188	9.48E-06	–-	rs933153	21	28 486 172	3.13 E-05	–-
rs1534446	6	154 625 192	9.88E-06	IPCEF1	rs1998450	1	86 745 177	3.30 E-05	LOC105378824
rs4129156	18	25 437 752	9.93E-06	–-	rs9367805	6	14 019 157	3.33 E-05	–-
rs14067	13	114 110 660	1.01E-05	DCUN1D2	rs1767282	1	112 357 101	3.40 E-05	KCND3
rs472276	1	244 112 606	1.02E-05	LOC339529	rs4490086	18	64 648 278	3.77 E-05	–-
rs9382934	6	14 040 480	1.16E-05	–-	rs13179953	5	11 179 193	3.89 E-05	CTNND2
rs2834077	21	34 422 738	1.32E-05	–-	rs522793	6	10 802 955	3.99 E-05	MAK
rs1852755	11	13 996 686	1.35E-05	SPON1	rs8095030	18	72 602 588	4.09 E-05	ZNF407
rs11640843	16	66 425 176	1.35E-05	CDH5	rs1078497	7	37 606 532	4.62 E-05	–-
rs10261484	7	22 583 326	1.37E-05	–-	rs6700343	1	150 149 016	4.69 E-05	LOC105371433

in the GSIS procedure at the 10^{-5} significance level. Moreover, the QQ plot displays the observed association $-\log_{10}(p)-$ values for all SNPs on the y-axis versus the expected uniform distribution of $-\log_{10}(p)-$ values under the null hypothesis of no association on the x-axis. As shown in Figure 4b, the observed $-\log_{10}(p)-$ values fit well with the expected $-\log_{10}(p)-$ values from the null hypothesis for most of the $-\log_{10}(p)-$ values. The $-\log_{10}(p)-$ values in the upper-right tail of the distribution actually show a significant deviation suggesting strong associations between these SNPs and the whole brain. Table 2 lists the top 50 SNPs associated with the whole brain, including the corresponding SNPs, chromosome (CHR) IDs, base pair (BP) values, *P*-values and gene. Among the top 50 SNPs, the following genes are detected: SPON1 is related to brain connections and implicated in many neurological and psychiatric disorders (Jahanshad *et al.*, 2013); CTNNA2 is associated with human cerebral cortex, and its loss in neurons leads to defects in neurite stability and migration (Schaffer *et al.*, 2018); CTNND2 is involved in neuronal development and closely related to chromatin biology (Turner *et al.*, 2015); and ZNF407 is linked to intellectual disability (Ren *et al.*, 2013).

For the detection procedure, the raw *P*-values of $W(g,v)$ are first calculated to detect significant voxel–locus pairs. N_0 is set as either 1000 or 2000, and the number of bootstrapped samples is fixed at 1000. At the 10^{-5} significance level, the number of significant voxel–locus pairs based on the raw *P*-values of $W\left(\tilde{g},v\right)$ against the top N_0 SNPs in $\tilde{G}_0$ is shown in Figure 5a and b. Figure 5c and d presents the number of significant voxel–locus pairs based on the corrected *P*-values of $W\left(\tilde{g},v\right)$ against the top $N_0=1000$ SNPs at 0.5 and 0.8 significance levels, respectively. Second, all possible clusters and their associated corrected *P*-values for the top $N_0=1000$ SNPs are calculated to detect significant cluster–locus pairs. The number of bootstrapped samples is fixed at 1000. Table 3 lists four selected SNPs, which have the four largest numbers of significant cluster–locus pairs at the 0.5 significance level.

Figure 6 shows some slices of $-\log_{10}(p)-$ values of significant clusters corresponding to a selected SNP (rs11891634). In Figure 6, symmetric clustering across the left and right hemispheres is inspected in the significant clusters. For most brain regions, brain structures are highly symmetric between hemispheres. Therefore, symmetric associations of SNPs and clusters can be biologically observed. Table 4 lists several major clusters and their corresponding SNPs in remarkable cluster–locus pairs detected by the proposed method. Among these clusters, hippocampus, olfactory cortex, parahippocampal gyrus, superior temporal gyrus, middle temporal gyrus, inferior temporal gyrus, amygdala, precuneus, fusiform, posterior cingulate and caudate nucleus are closely related to AD (Ning *et al.*, 2018; Weiner *et al.*, 2015).

5 Conclusion and discussion

In this study, a novel VGWAS method was proposed, and the following contributions were presented. First, the modification of the SLIC method was introduced to spatial grouping in an anatomically meaningful manner. Second, a SASM was incorporated into the VGWAS framework to increase the power of detecting potential AD biomarkers. Third, the detected biomarkers were used as predictors to classify AD/NC subjects and could create a link to AD. The proposed method was evaluated on a total of 193 275 voxels and 501 584 SNPs. Experimental results showed that the proposed method had the potential to detect some AD-related biomarkers and achieved high accuracy in AD/NC classification. Therefore, the proposed method was a useful tool for AD prediction, diagnosis and monitoring.

In the proposed method, K is a crucial parameter used to determine the size of $N(v)$ for each v. In general, a small K corresponds

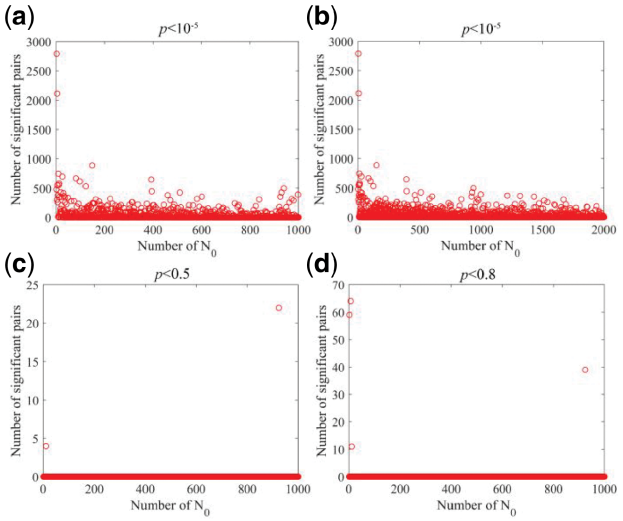

Fig. 5. ADNI whole-brain VGWAS: the number of significant voxel–locus pairs based on the raw *P*-values of $W(\tilde{g}, v)$ at the 10^{-5} significance level corresponding to the top (**a**) $N_0 = 1000$ and (**b**) $N_0 = 2000$ SNPs; the number of significant voxel–locus pairs based on the corrected *P*-values of $W(\tilde{g}, v)$ at (**c**) 0.5 and (**d**) 0.8 significance levels corresponding to the top $N_0 = 1000$ SNPs

Table 3. ADNI whole-brain VGWAS: significant cluster–locus pairs at 0.5 significance level

SNP	Number of cluster–locus pairs	Max cluster size	*P*-value of the max cluster
rs11891634	1	12 117	0.16
rs2480271	1	11 428	0.33
rs7001339	1	11 077	0.47
rs12001550	1	11 321	0.37

to a large supervoxel and causes a smooth effect on a contiguous region. However, brain MRI images are usually expected to contain spatially contiguous regions or effect regions with relatively sharp edges (Huang *et al.*, 2015; Zhu *et al.*, 2014). A small K may also smoothen sharp edges in some instances. Moreover, optimizing K is difficult because no evidence supports the ground truth of AD biomarkers in imaging and genetic data. In this study, AD/NC classification accuracy was used as the measurement to select the optimized K. The classification accuracy achieved the highest score when $K = 2000$. Therefore, a moderate-sized K was more suitable for considering spatially contiguous regions and effect regions with relatively sharp edges in the proposed method than other K values.

In most existing VGWAS methods, imaging phenotypes are used as traits to directly identify phenotype-associated genetic data. However, the identified genetic data and the used imaging data may or may not be associated with diseases (e.g. AD in this study), and further studies should be performed to confirm or refute a suggestive link to a disease (Xu *et al.*, 2017). In our study, we applied the detected imaging and genetic biomarkers as predictors for AD/NC classification, considering that the accurate prediction and diagnosis of AD were the final targets of AD-associated biomarker detection. In Table 1, all of the classification accuracy measurements of the proposed method with spatial–anatomical correlations were higher than those of the FVGWAS method, indicating the effectiveness of incorporating spatial–anatomical correlations into the proposed method. We used either a cluster or a SNP as a predictor instead of

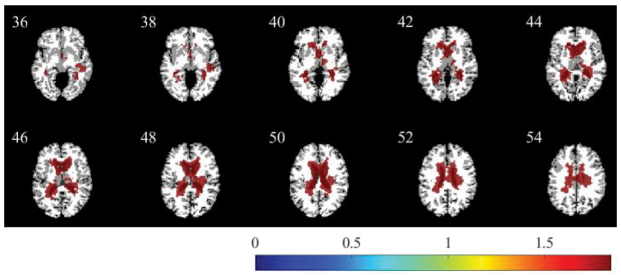

Fig. 6. ADNI whole-brain VGWAS: selected slices of $-log_{10}(p)$ – values for significant clusters corresponding to a SNP (rs11891634)

combining them as predictors in this experiment because the detected clusters and SNPs were considerably associated with one another, indicating that redundant information may be present between them. Therefore, combining clusters and SNPs elicited few effects on improving the classification accuracy. However, the accuracy of the proposed method with cluster as a predictor (AUC = 0.952 ± 0.012) was comparable with that of several recently proposed AD classification methods (Ning *et al.*, 2018; Zhuo *et al.*, 2018). The accuracy of the proposed method with SNP as a predictor outperformed some relevant methods (Ning *et al.*, 2018; Zhang *et al.*, 2014), which also involve SNP as a predictor to classify subjects into AD and NC.

In the biomarker detection experiments, some new risk genes and clusters were found, and they might be beneficial to the early prediction, diagnosis and treatment of AD. Among the top 50 SNPs listed in Table 2, the following genes were detected: SPON1 (CHR 11), which is related to neurological and psychiatric disorders; CTNNA2 (CHR 2), which is associated with the human cerebral cortex; CTNND2 (CHR 5), which is implicated in neuronal development and closely related to chromatin biology and ZNF407 (CHR 18), which is associated with intellectual disability. Therefore, these genes are considerably linked to the occurrence of AD. Structural changes related to the subregions of the brain as detected by our proposed method might be affected by the progression of AD (Table 4). The hippocampus, the olfactory cortex and the parahippocampal gyrus are connected to memory. The superior temporal gyrus is associated with sound and speech processing. The middle temporal gyrus is related to writing and reading. The inferior temporal gyrus is one of the higher levels of the ventral stream of visual processing and associated with the representation of complex object features. The amygdala plays a primary role in the processing of memory, decision-making and emotional responses. The precuneus is involved with episodic memory, visuospatial processing, reflections upon self and aspects of consciousness. The fusiform is associated with color recognition, word and body recognition. The posterior cingulate is linked to emotion and memory. The caudate nucleus is relative to memory and learning, and is found to have a significant volume reduction in patients with AD (Jiji *et al.*, 2013).

Several issues should be addressed in our future research. First, the proposed method is still a single SNP analysis framework (Huang *et al.*, 2015, 2017). As such, the power of VGWAS may be undermined by unobserved causal SNPs, correlation between adjacent SNPs and SNP–SNP interactions (Greenlaw *et al.*, 2017; Wang *et al.*, 2012). Analyzing the association between a single SNP set and individual phenotypes may help improve the power of VGWAS (Thompson *et al.*, 2013). Therefore, the proposed method should be extended to the analysis of the association between a SNP set and the whole brain. Second, considering that various characteristics of

Table 4. Major clusters and their corresponding SNPs in significant cluster–locus pairs detected by the proposed method

SNP	Cluster
rs11891634	Rolandic operculum right; Insula left/right; Anterior cingulate and paracingulate gyri right; Posterior cingulate gyrus left/right; Hippocampus left/right; Parahippocampal gyrus right; Calcarine fissure and surrounding cortex left/right; Lingual gyrus left/right; Fusiform gyrus right; Precuneus left/right; Caudate nucleus left/right; Lenticular nucleus putamen right; Thalamus left/right; Middle temporal gyrus right
rs2480271	Olfactory cortex left/right; Anterior cingulate and paracingulate gyri right; Hippocampus left/right; Parahippocampal left/right; Calcarine fissure and surrounding cortex right; Lingual gyrus left; Superior occipital gyrus left; Precuneus left/right; Caudate nucleus left/right; Lenticular nucleus putamen left; Lenticular nucleus pallidum left; Thalamus left/right; Heschl gyrus right
rs7001339	Inferior frontal gyrus orbital part right; Olfactory cortex right; Insula left; Anterior cingulate and paracingulate gyri left; Median cingulate and paracingulate gyri right; Posterior cingulate gyrus left/right; Hippocampus left/right; Parahippocampal gyrus right; Calcarine fissure and surrounding cortex left; Caudate nucleus left/right; Thalamus left/right
rs12001550	Rolandic operculum left; Olfactory cortex left/right; Insula right; Median cingulate and paracingulate gyri right; Posterior cingulate gyrus left; Hippocampus left/right; Amygdala right; Calcarine fissure and surrounding cortex left; Lingual gyrus left; Fusiform gyrus right; Precuneus left/right; Caudate nucleus left/right; Lenticular nucleus putamen left/right; Lenticular nucleus pallidum left/right; Thalamus left/right; Heschl gyrus left; Superior temporal gyrus right; Inferior temporal gyrus right

image phenotypes can be obtained from different neuroimaging modalities (e.g. functional MRI, PET and diffusion tensor imaging), we may achieve better results when different image phenotypes are combined with our research. Third, the proposed method can be used to detect genetic biomarkers that affect neuroimaging phenotypes. Some AD-associated latent factors, such as education level (Frost *et al.*, 2016) and memory scores (Yan *et al.*, 2015), have been completely disregarded in this study. However, incorporating these factors within genome-wide data can be challenging because of the loss in statistical power and computational efficiency (Huang *et al.*, 2017). Therefore, our proposed method should be extended to the evaluation of the effects of these factors.

Funding

This work was supported by the Science and Technology Planning Project of Guangdong [grant number 201904010417] Province, China [grant number 2015B010131011]; Major Program of National Natural Science Foundation of China [grant number U15012561016942]; Science and Technology Planning Project of Guangzhou [grant number 201904010417]; and National Natural Science Foundation of China [NSFC, grant number 81601562]. Data collection and sharing for this project was funded by ADNI [National Institutes of Health Grant U01 AG024904]; and DOD ADNI [Department of Defense award number W81XWH-12-2-0012].

Conflict of Interest: none declared.

References

Achanta,R. *et al.* (2012) SLIC superpixels compared to state-of-the-art superpixel methods. *IEEE Trans. Pattern Anal. Mach. Intell.*, **34**, 2274–2282.

Alzheimer's Association (2016) 2016 Alzheimer's disease facts and figures. *Alzheimers Dement.*, **12**, 459–509.

Chauhan,G. *et al.* (2015) Association of Alzheimer's disease GWAS loci with MRI markers of brain aging. *Neurobiol. Aging*, **36**, 1765.e7–1765.e16.

Davatzikos,C. *et al.* (2001) Voxel-based morphometry using the RAVENS maps: methods and validation using simulated longitudinal atrophy. *Neuroimage*, **14**, 1361–1369.

Fan,Y. *et al.* (2007) COMPARE: classification of Morphological Patterns Using Adaptive Regional Elements. *IEEE Trans. Med. Imaging*, **26**, 93–105.

Frisoni,G.B. *et al.* (2010) The clinical use of structural MRI in Alzheimer disease. *Nat. Rev. Neurol.*, **6**, 67–77.

Frost,H.R. *et al.* (2016) Identifying significant gene-environment interactions using a combination of screening testing and hierarchical false discovery rate control. *Genet. Epidemiol.*, **40**, 544–557.

Greenlaw,K. *et al.* (2017) A Bayesian group sparse multi-task regression model for imaging genetics. *Bioinformatics*, **33**, 2513–2522.

Huang,C. *et al.* (2017a) FGWAS: functional genome wide association analysis. *Neuroimage*, **159**, 107–121.

Huang,M. *et al.* (2019) Spatial correlations exploitation based on nonlocal voxel-wise GWAS for biomarker detection of AD. *NeuroImage Clin.*, **21**, 101642.

Huang,M. *et al.* (2015) FVGWAS: fast voxelwise genome wide association analysis of large-scale imaging genetic data. *Neuroimage*, **118**, 613–627.

Huang,M. *et al.* (2017b) Longitudinal Measurement and Hierarchical Classification Framework for the Prediction of Alzheimer's Disease. *Sci. Rep.*, **7**, 39880.

Jahanshad,N. *et al.* (2013) Genome-wide scan of healthy human connectome discovers SPON1 gene variant influencing dementia severity. *Proc. Natl. Acad. Sci. USA*, **110**, 4768–4773.

Jiji,S. *et al.* (2013) Segmentation and volumetric analysis of the caudate nucleus in Alzheimer's disease. *Eur. J. Radiol.*, **82**, 1525–1530.

Lambert,J.C. *et al.* (2013) Meta-analysis of 74, 046 individuals identifies 11 new susceptibility loci for Alzheimer's disease. *Nat. Genet.*, **45**, 1452–1458.

Li,Y. *et al.* (2012) TwinMARM: two-stage multiscale adaptive regression methods for twin neuroimaging data. *IEEE Trans. Med. Imaging*, **31**, 1100–1112.

Li,Y.M. *et al.* (2013) Multiscale adaptive generalized estimating equations for longitudinal neuroimaging data. *Neuroimage*, **72**, 91–105.

Liu,M. *et al.* (2015) View-centralized multi-atlas classification for Alzheimer's disease diagnosis. *Hum. Brain Mapp.*, **36**, 1847–1865.

Mattsson,N. *et al.* (2009) CSF biomarkers and incipient Alzheimer disease in patients with mild cognitive impairment. *JAMA*, **302**, 385–393.

Ning,K.D. *et al.* (2018) Classifying Alzheimer's disease with brain imaging and genetic data using a neural network framework. *Neurobiol. Aging*, **68**, 151–158.

Rathore,S. *et al.* (2017) A review on neuroimaging-based classification studies and associated feature extraction methods for Alzheimer's disease and its prodromal stages. *Neuroimage*, **155**, 530–548.

Ren,C.M. *et al.* (2013) Balanced translocation t(3; 18)(p13; q22.3) and points mutation in the ZNF407 gene detected in patients with both moderate non-syndromic intellectual disability and autism. *Biochim. Biophys. Acta Mol. Basis Dis.*, **1832**, 431–438.

Santi,S.D. *et al.* (2001) Hippocampal formation glucose metabolism and volume losses in MCI and AD. *Neurobiol. Aging*, **22**, 529–539.

Schaffer,A.E. *et al.* (2018) Biallelic loss of human CTNNA2, encoding alpha N-catenin, leads to ARP2/3 complex overactivity and disordered cortical neuronal migration. *Nat. Genet.*, **50**, 1093–1101.

Shen,D. and Davatzikos,C. (2004) Measuring temporal morphological changes robustly in brain MR images via 4-dimensional template warping. *Neuroimage*, **21**, 1508–1517.

Sled,J.G. *et al*. (1998) A nonparametric method for automatic correction of intensity nonuniformity in MRI data. *IEEE Trans. Med. Imaging*, **17**, 87–97.

Stein,J.L. *et al*. (2010) Voxelwise genome-wide association study (vGWAS). *Neuroimage*, **53**, 1160–1174.

Thompson,P.M. *et al*. (2013) Genetics of the connectome. *Neuroimage*, **80**, 475–488.

Turner,T.N. *et al*. (2015) Loss of delta-catenin function in severe autism. *Nature*, **520**, 51–56.

Tzourio-Mazoyer,N. *et al*. (2002) Automated anatomical labeling of activations in SPM using a macroscopic anatomical parcellation of the MNI MRI single-subject brain. *Neuroimage*, **15**, 273–289.

Wang,H. *et al*. (2012) Identifying quantitative trait loci via group-sparse multitask regression and feature selection: an imaging genetics study of the ADNI cohort. *Bioinformatics*, **28**, 229–237.

Wang,J. *et al*. (2016) Parcellating Whole Brain for Individuals by Simple Linear Iterative Clustering. In: *International Conference on Neural Information Processing*. pp. 131–139.

Wang,Y. *et al*. (2014) Knowledge-guided robust MRI brain extraction for diverse large-scale neuroimaging studies on humans and non-human primates. *PLoS One*, **9**, e77810.

Weiner,M.W. *et al*. (2015) 2014 Update of the Alzheimer's Disease Neuroimaging Initiative: a review of papers published since its inception. *Alzheimers Dement*., **11**, e1–e120.

Xu,Z. *et al*. (2017) Imaging-wide association study: integrating imaging endophenotypes in GWAS. *Neuroimage*, **159**, 159–169.

Yan,J.W. *et al*. (2015) Hippocampal transcriptome-guided genetic analysis of correlated episodic memory phenotypes in Alzheimer's disease. *Front. Genet*., **6**, 117.

Zhang,Y. *et al*. (2001) Segmentation of brain MR images through a hidden Markov random field model and the expectation-maximization algorithm. *IEEE Trans. Med. Imaging*, **20**, 45–57.

Zhang,Z.M. *et al*. (2014) Integrative analysis of multi-dimensional imaging genomics data for Alzheimer's disease prediction. *Front. Aging Neurosci*., **6**, 260.

Zhu,H.T. *et al*. (2014) Spatially Varying Coefficient Model for Neuroimaging Data with Jump Discontinuities. *J. Am. Stat. Assoc*., **109**, 1084–1098.

Zhu,H.T. *et al*. (2012) Multivariate Varying Coefficient Model for Functional Responses. *Ann. Stat*., **40**, 2634–2666.

Zhuo,S. *et al*. (2018) Integrating spatial-anatomical regularization and structure sparsity into SVM: improving interpretation of Alzheimer's disease classification. *Neuroimage*, **178**, 445–460.